Heliyon 10 (2024) e40818

Contents lists available at ScienceDirect

Heliyon

journal homepage: www.cell.com/heliyon

Research article

Antibacterial activity of copper-decorated CeO_2 nanoparticles and preparation of antifouling polyethersulfone surface

Lokman Şener [a], Sadin Özdemir [b], M. Serkan Yalçın [c], Mehmet Gülcan [a,*], Nadir Dizge [d,**,1]

[a] Food Processing Programme, Technical Science Vocational School, Mersin University, 33343, Yenisehir, Mersin, Turkey
[b] Department of Chemistry and Chemical Processing Technologies, Technical Science Vocational School, Mersin University, 33343, Mersin, Turkey
[c] Department of Chemistry, Faculty of Science, Van Yüzüncü Yıl University, Van, 65080, Turkey
[d] Department of Environmental Engineering, Faculty of Engineering, Mersin University, 33343, Yenisehir, Mersin, Turkey

ARTICLE INFO

Keywords:
Antimicrobial
Biofilm inhibition
Cerium oxide NPs
DNA cleavage
PES membrane

ABSTRACT

Cerium oxide NPs (*nano*-CeO_2), with notable performance in various biological tests like redox activity, free radical scavenging, and biofilm inhibition, emerge as significant candidates to address issues in related areas. In this research, copper-decorated *nano*-CeO_2 (Cu@*nano*-CeO_2) were first synthesized and then characterized using advanced techniques such as SEM-EDX, XRD, XPS, BET, and ICP-OES. The biochemical properties of the obtained Cu@*nano*-CeO_2 nanostructure and its performance in polyethersulfone (PES) membranes were thoroughly investigated in this research study. The free radical scavenging effect of Cu@*nano*-CeO_2 at 100 mg/L concentration was determined as 100 % with the same activity as the reference compounds Trolox and ascorbic acid. It enhanced 2.9-fold α-amylase enzyme activity at 50 mg/L. Plasmid DNA was completely degraded at 100 mg/L concentration. Cu@*nano*-CeO_2 provided significant inhibition against tested bacterial and fungal strains, especially Gram-positives than Gram-negatives and fungus. Anti-biofilm activity was determined against *S. aureus* and *P. aeruginosa* as 98.3 and 82.1 %, respectively. Furthermore, *E. coli* inhibition activity of PES/Cu@*nano*-CeO_2 1.0 wt% membrane was determined as 100 %. Owing to the promising results obtained, we can suggest that Cu@*nano*-CeO_2 can be used in wastewater treatment.

1. Introduction

Cerium (Ce) is one of the best elements representing rare earth elements due to its unique chemical/physical properties and distinctive outer electron configuration ($[Xe]4f^15d^16s^2$). Its abundant presence in the Earth's crust (66.5 ppm) has made the utilization of Ce-based compounds notably prominent in recent years due to their price advantage. Ce compounds find applications in various industrial sectors including magnets, alloys, and catalysis. Among these Ce compounds, cerium oxide (CeO_2) has garnered the most interest as a star material in academic research or practical fields [1,2]. CeO_2 nanoparticles (NPs) have particularly attracted intense interest in nanotechnology due to their beneficial applications as catalysts, fuel cells, and antioxidants in biological systems [3–6].

* Corresponding author.
** Corresponding author.
E-mail addresses: mehmetgulcan@yyu.edu.tr (M. Gülcan), nadirdizge@gmail.com (N. Dizge).
[1] http://aves.yyu.edu.tr/mehmetgulcan/.

https://doi.org/10.1016/j.heliyon.2024.e40818
Received 24 June 2024; Received in revised form 27 November 2024; Accepted 28 November 2024
Available online 29 November 2024

Generally, cerium is known to exist in two oxidation states: Ce^{3+} and Ce^{4+}. Therefore, cerium dioxide can exist in two different oxide forms in bulk material: CeO^2 (Ce^{4+}) or Ce_2O_3 (Ce^{3+}) [7,8]. At the nano scale, cerium oxide possesses a cubic fluorite structure, and both Ce^{3+} and Ce^{4+} can coexist on its surface. The presence of Ce^{3+} leads to a charge deficiency compensated by oxygen vacancies within the cage, thus CeO_2-NPs inherently contain oxygen defects [9]. These oxygen defects are actually designated as active sites for catalytic activities. As the particle size decreases, the concentration of oxygen defects increases, thereby CeO_2-NPs exhibit enhanced redox properties compared to bulk materials [10]. Additionally, it's noted in the literature that the presence of mixed valence states plays a significant role in the removal of reactive oxygen and nitrogen species. Furthermore, it has been found that CeO_2-NPs are effective against pathologies associated with chronic oxidative stress and inflammation. However, recently, it has been reported that CeO_2-NPs exhibit fascinating properties as a material with multiple enzyme-like activities, including superoxide dismutase, catalase, and oxidase, in very important biological areas such as bioanalysis, biomedicine, and drug delivery [8,11–16]. It is known that all these applications are derived from the rapid transition between the oxidation states of Ce^{3+} and Ce^{4+} [7]. The surface Ce^{3+}:Ce^{4+} ratio is influenced by the microenvironment. Therefore, the adopted microenvironment and synthesis method also play an important role in determining the biological activity and toxicity of CeO_2-NPs. Literature studies indicate that solution precipitation, sonochemical, hydrothermal, solvothermal, ball milling, thermal decomposition, spray pyrolysis, thermal hydrolysis, and sol-gel methods are used to synthesize CeO_2-NPs [8,14–16].

Nanomaterials, defined as structures ranging from 1 nm to 100 nm, are being investigated in various scientific fields such as physics, chemistry, biology, medicine, pharmacy, and materials science due to their different optical and electronic properties from their bulk counterparts [17–19]. Reducing the particle size unveils the superior characteristics of these materials, enabling the development of new and advanced applications in fields such as communication, energy storage, sensing, data storage, optics, transmission, environmental protection, cosmetics, biology, and medicine. In recent years, significant efforts have been made to produce many nanomaterials with controlled morphologies, shapes, and sizes [15]. Metal NPs, which have a higher surface-to-volume ratio compared to their bulk counterparts, contain more catalytically active atoms on their surfaces. Thus, the wide surface areas and high surface energies make metal NPs thermodynamically unstable against aggregation in bulk form. In this context, suitable protective ligands or polymers are widely used in their synthesis to prevent their aggregation. However, even in the presence of the best stabilizing agents, the eventual agglomeration of metal NPs into bulk remains the most critical issue that needs to be overcome in applications. Additionally, obtaining pure active metal surfaces by avoiding surface contamination from surface-protecting groups, which often leads to reduced effectiveness due to the blocking of active sites, is another critical issue. In this regard, using porous and nano-sized support materials as host materials for the immobilization of guest metal NPs allows the production of active sites without specific surface-active substances, along with the advantages of preventing particle aggregation [20–22].

The general definition of membrane fouling is the accumulation and deposition of unwanted elements inside or on the surface of membranes. Particles in solution, partially soluble organic and/or inorganic macromolecules, and/or biological microorganisms could all be among the materials that have been deposited. Membrane fouling, thus, is an inevitable phenomenon in membrane-based water treatment processes and can seriously harm the processes' functionality, sustainability, and viability from an economic standpoint. The numerous physical and chemical interactions that occur between the membrane surface and different feed contents result in fouling mechanisms [23–25]. Foulant deposition and fouling layer formation are significantly influenced by the properties of the membrane surface, such as charge, chemistry, hydrophobicity/hydrophilicity, and shape [26]. Therefore, modifying these attributes through a suitable membrane surface modification technique offers the most effective means of enhancing the antifouling performance of membranes. Common surface modification techniques encompass reducing the roughness of the membrane surface, enhancing its hydrophilicity, and introducing antiadhesive monomers, polymers, or nanoparticles onto the membrane surface [27–31]. The development of antifouling coatings for membranes has benefited substantially from current developments in nanotechnology, polymer science, and biomimetic surface design. In order to enhance the antifouling capabilities of membranes, metal and metal oxide nanoparticles (NPs) such as Ag, Fe_3O_4, TiO_2, and WS_2 have been employed in membrane manufacture and/or modification during the last decade. Additionally, carbon-based nanomaterials such as CNTs, graphene, GO, and polymeric NPs have attracted intensive research interests in the antifouling capabilities of membranes [32].

Motivated by the superior properties of cerium oxide and metal nanoparticles outlined above, in this research study, copper-decorated *nano*-CeO_2 (Cu@*nano*-CeO_2) was first prepared and characterized using a combination of various techniques. Subsequently, the biochemical properties and the performance of polyethersulfone (PES) membrane of Cu@*nano*-CeO_2 nanostructure were investigated.

2. Materials and method

2.1. Materials

Copper (II) chloride dihydrate ($CuCl_2 \bullet 2H_2O$), cerium (IV) oxide (CeO_2; nanopowder, <25 nm particle size), and N-methyl-2-pyrrolidine (NMP) were acquired from Sigma-Aldrich for experimental investigations and were utilized without prior treatment. Polyethersulfone (PES) used as a polymer (Ultrasound E 6020 P) was kindly provided form BASF Company in Turkey. Likewise, all solvents employed in the experimental studies were of high purity, obviating the need for preliminary purification.

2.2. Synthesis of Cu@nano-CeO_2

The decoration of Cu NPs on the *nano*-CeO_2 surface was carried out through wet impregnation-reduction steps [33,34]. For this

purpose, a solution of $CuCl_2 \bullet 2H_2O$ salt containing 2 % Cu metal was mixed with *nano*-CeO_2 at 298 K and 750 rpm for approximately 4 h. Then, an aqueous solution of $NaBH_4$ was added to the mixture to reduce the Cu metals on the *nano*-CeO_2 surface. After the reduction process was completed, the mixture was centrifuged to isolate the solid part. The solid product was washed several times with water to remove potential impurities and then dried overnight in a vacuum oven set at 80 °C.

2.3. Synthesis of Cu@nano-CeO_2 blended PES membrane

PES membranes both pristine and functionalized were synthesized using the phase inversion approach. Initially, PES beads were dried at 70 °C in an oven for 2 h. After that, Cu@*nano*-CeO_2 were dissolved uniformly in the NMP solvent for 10 min in an ultrasonic water bath and PES beads were added to the final mixture. Overnight at 60 °C in an incubator, PES beads were allowed to dissolve completely in the solution while being shaken. Additionally, PES beads (14 %, w/w) were dissolved in NMP solvent at 60 °C to prepare the casting solution for the pristine membrane. In order to synthesis blended composite membranes, Cu@*nano*-CeO_2 was added to the casting solution at varying weight percentages (0.5, 1.0, and 2.0 wt%) Then, air bubbles were eliminated from the polymer solution by sonicating it for duration of 20 min. A 200 μm thick casting blade was used to disseminate the bubble-free membrane solutions at a speed of 100 mm/s across the glass layer. To precipitate the polymer, the glass plate was immerged in a coagulation bath containing deionized water. After the polymer was precipitated by immersing the glass plate in a coagulation bath with deionized water, the membranes were phase-transformed and the residual solvent was removed by immersing the plate in distilled water for at least an overnight.

2.4. Characterization

The characterization of the Cu@*nano*-CeO_2 nanostructure involved several techniques. A Zeiss Sigma 300 scanning electron microscope was utilized for scanning electron microscopy (SEM) and scanning electron microscopy-energy dispersive X-ray spectroscopy (SEM-EDX) analyses. PANalytical Empyrean X-ray diffractometer with Cu-Kα radiation (wavelength 1.54 Å, 40 kV, 55 mA) was employed for obtaining P-XRD patterns. Surface chemistry details of the Cu@*nano*-CeO_2 nanostructure were acquired using a Kratos AXIS Ultra spectrometer for XPS analysis with monochromatic Al-Kα radiation (1486.6 eV, the X-ray tube operating at 15 kV and 350 W, and pass energy of 23.5 eV). The C 1s photoelectron line (binding energy = 284.6 eV) was employed for calibrating the binding energies of the photoelectron. Brunauer-Emmett–Teller (BET) N_2 adsorption-desorption analyses were conducted at 77 K using a Micrometrics Surface Area and Porosity instrument (MicroActive for TriStar II 3020 V1.04). The Cu metal content in the Cu@*nano*-CeO_2 nanostructure was assessed through inductively coupled plasma optical emission spectrometry (ICP-OES) analysis on a PerkinElmer Optima 4300DV ICP emission spectrometer. Prior to ICP-OES analysis, each sample underwent complete dissolution in a mixture of HNO_3/HCl (1/3; v/v).

2.5. DPPH radical scavenging assay of Cu@nano-CeO_2

The method as described by Blois [35] was applied to assess the antioxidant capability of the Cu@*nano*-CeO_2 based on the scavenging of stable 2,2-diphenyl-1-picrylhydrazyl (DPPH) free radical. While a negative control containing reagents except the sample was used, ascorbic acid and Trolox were used as the positive control. 250 μL different concentrations of sample and controls were transferred into test tubes followed by the addition of 1 mL of DPPH (0.002 %) solution. These test tubes were shaken vigorously and then incubated at room temperature for about 30 min with no light exposure. To determine the inhibition, spectrophotometric analysis at 517 nm was applied to calculate the percentage of free radical scavenging activity (%FRSA). The given following formula was used to compute the FRSA.

$$\text{FRSA}\ (\%) = \left(\text{Abs}_{(\text{control})} - \text{Abs}_{(\text{sample})} \,/\, \text{Abs}_{(\text{control})}\right) \times 100$$

2.6. Effect of Cu@nano-CeO_2 on α-amylase activity

Various concentrations of the sample at 50, 100 and 200 mg/L were poured into the test tubes. Then phosphate buffer and α-amylase were added and incubated at 37 °C for 15 min. 0.2 mL 2 % potato starch solution was added to initiate the hydrolysis process at 37 °C for 20 min. After the incubation, 0.4 mL 3,5-dinitro salicylic acid (DNS) was added to each test tube to terminate the hydrolysis process. The tubes were then boiled at 100 °C for 5 min. After the mixture cooled, dilution was made using 3 mL distilled water, and spectrophotometric measurements of the mixture were made at 540 nm. The solution without test samples was used as a control. The α-amylase activity was calculated according to the formula below.

$$\alpha - \text{amylase activity}(\%) = \left(\text{Abs}_{(\text{control})} - \text{Abs}_{(\text{sample})} \,/\, \text{Abs}_{(\text{control})}\right) \times 100$$

2.7. DNA nuclease experiments of Cu@nano-CeO_2

The DNA nuclease activity of the Cu@*nano*-CeO_2 was performed using DNA agarose gel electrophoresis studies which is a common laboratory technique used to separate and analyze DNA, RNA, and proteins based on their size and charge. The assays were carried out using pBR322 plasmid DNA. The DNA was treated with increasing concentrations of the sample (50, 100, 200 mg/L) and incubated at

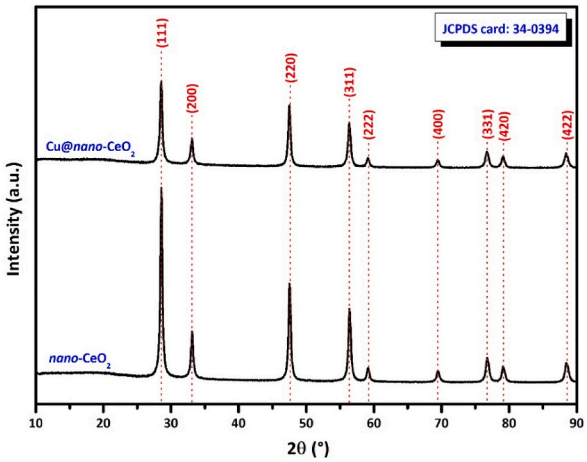

Fig. 1. XRD patterns of *nano*-CeO_2 and Cu@*nano*-CeO_2 samples.

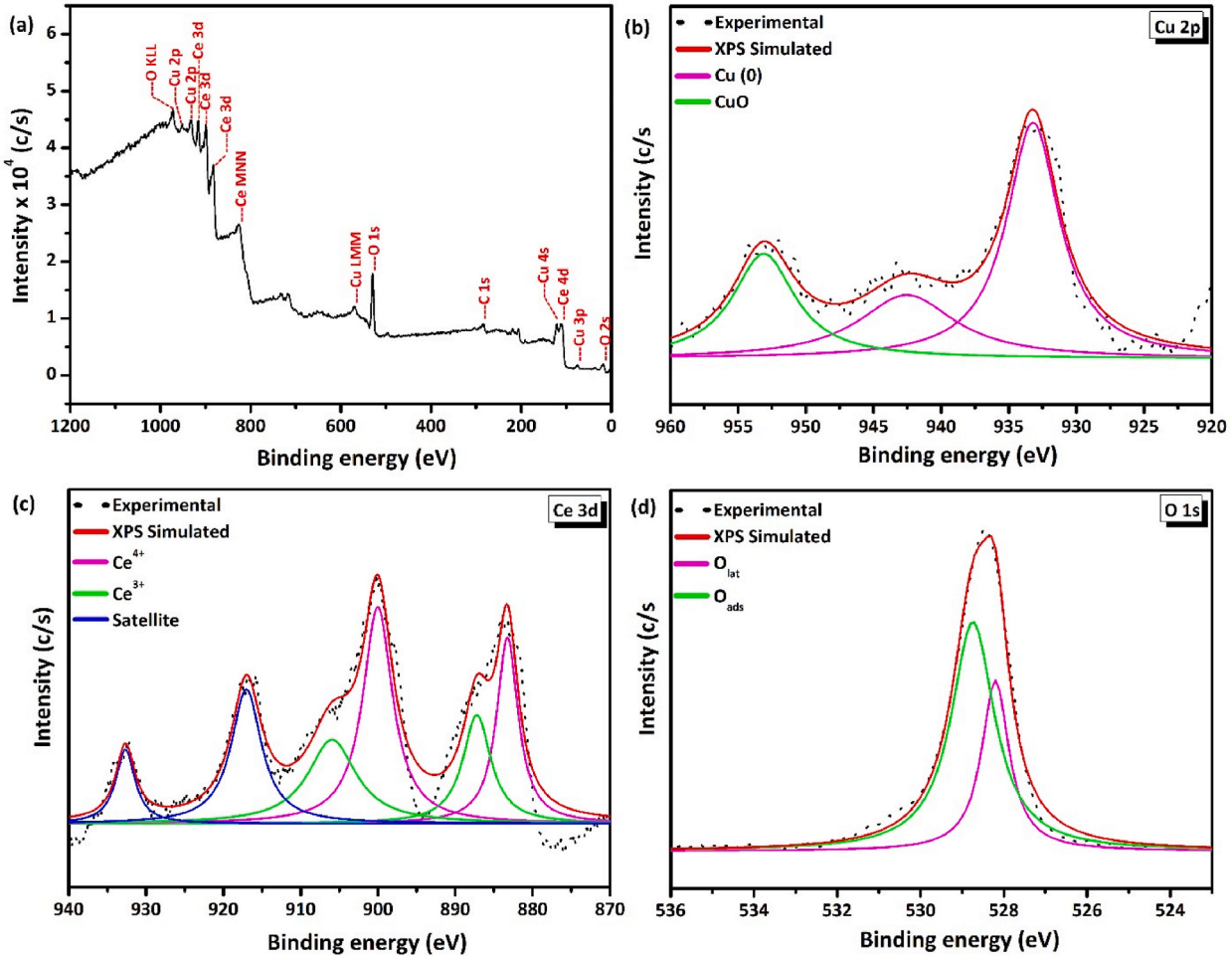

Fig. 2. Survey (a), Cu 2p (b), Ce 3d (c), and O 1s (d) core levels XPS spectra of Cu@*nano*-CeO_2 nanostructure.

37 °C for 90 min. Then, the 10 × loading buffer was added to the electrophoresis apparatus, and samples were loaded onto an agarose gel (1.0 % w/v) and stained with 0.5 μg/mL EthBr. Electrophoresis was run at 100 V in a Tris-acetic acid-EDTA buffer for 1.5 h. Negative control was applied using untreated plasmid DNA. Finally, the electrophoresis bands were photographed under the UV

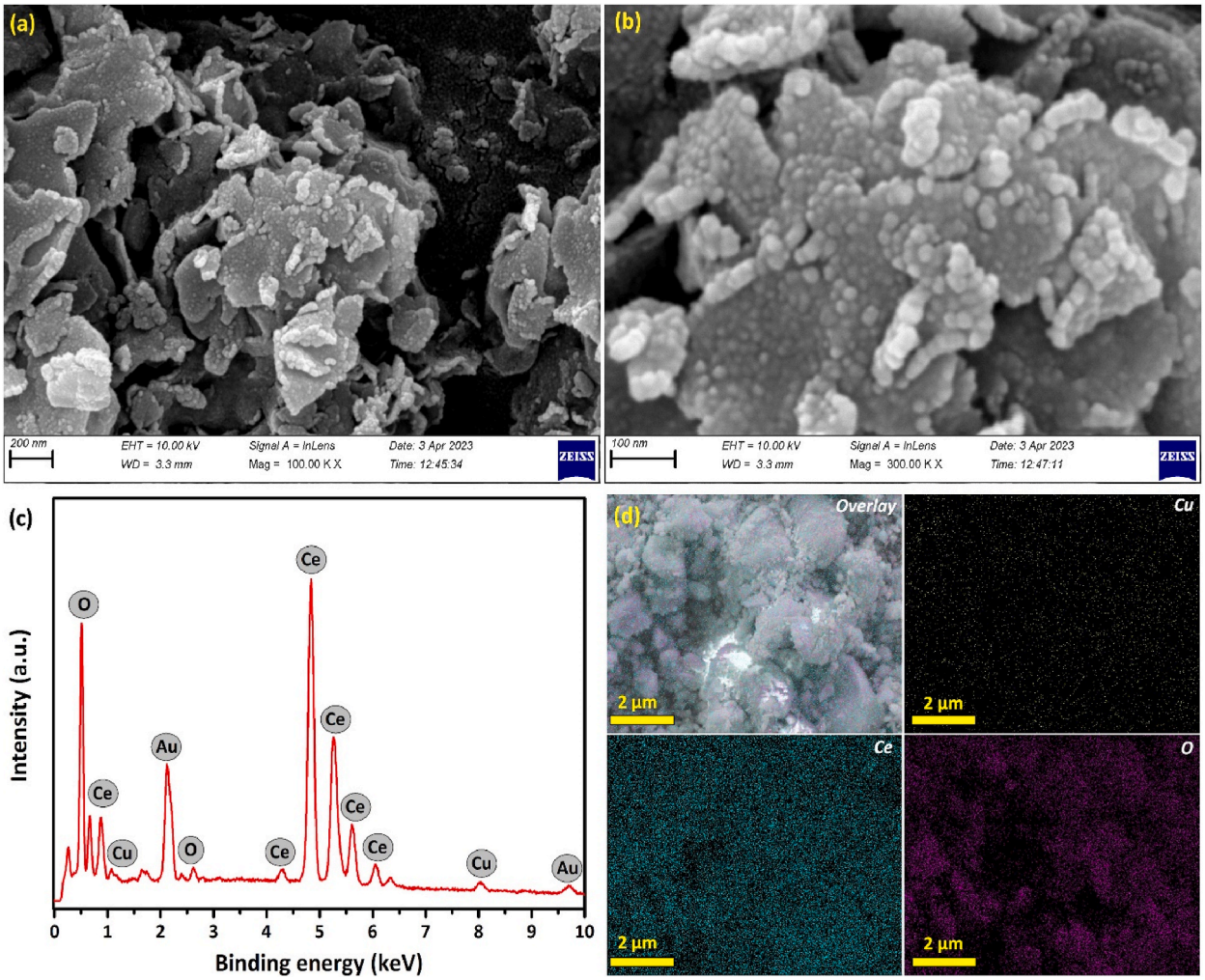

Fig. 3. SEM images in different scale (a–b), SEM-EDX spectrum (c), and SEM-elemental mapping (d) of Cu@*nano*-CeO_2 nanostructure.

illuminator.

2.8. Antimicrobial assays of Cu@nano-CeO_2

The standard broth microdilution method was applied. Different bacterial and fungal strains were used for the antimicrobial assay such as three Gram-negative bacteria *Escherichia coli* (ATCC 25922), *Legionella pneumophila* subsp. *pneumophila* (ATCC 33152), and *Pseudomonas aeruginosa* (ATCC 27853); and three Gram-positive bacteria *Enterococcus faecalis* (ATCC 29212), *Enterococcus hirae* (ATCC 10541), and *Staphylococcus aureus* (ATCC 25923); and two fungus *Candida tropicalis* (ATCC 750) and *Candida albicans*. These species were inoculated into a 10 µL aliquot of sterile Nutrient Broth for refreshing and grown at 37 °C overnight before the application. The desired concentration of Cu@*nano*-CeO_2 was poured into the first well of a microplate containing nutrients. Serial dilution of the samples was applied to the other wells. Each well was then inoculated with approximately 1.5 x 10^8 CFU/mL of microorganisms. During 24 h at 37 °C microplates were incubated on a shaker. In the end, minimum inhibition concentration (MIC) values were determined.

2.9. Microbial cell viability test of Cu@nano-CeO_2

The bacterial cell viability inhibition capacity of Cu@*nano*-CeO_2 was assessed using a model strain *E. coli* (ATCC 25922). *E. coli* was grown in an appropriate medium at 37.0 °C for one day using a shaker. Bacterial cells were separated by centrifugation and cleaned with a sterile saline solution to remove the contaminant. Cell viability test was applied after exposing *E. coli* to varying concentrations of Cu@*nano*-CeO_2 at 37 °C for 2 h. Posttreatment, *E. coli* inoculated on agar medium and left to incubate for one day at 37 °C. Percentile cell viability was calculated following formula using the ratio of colonies number after exposure to Cu@*nano*-CeO_2 to the non-exposed

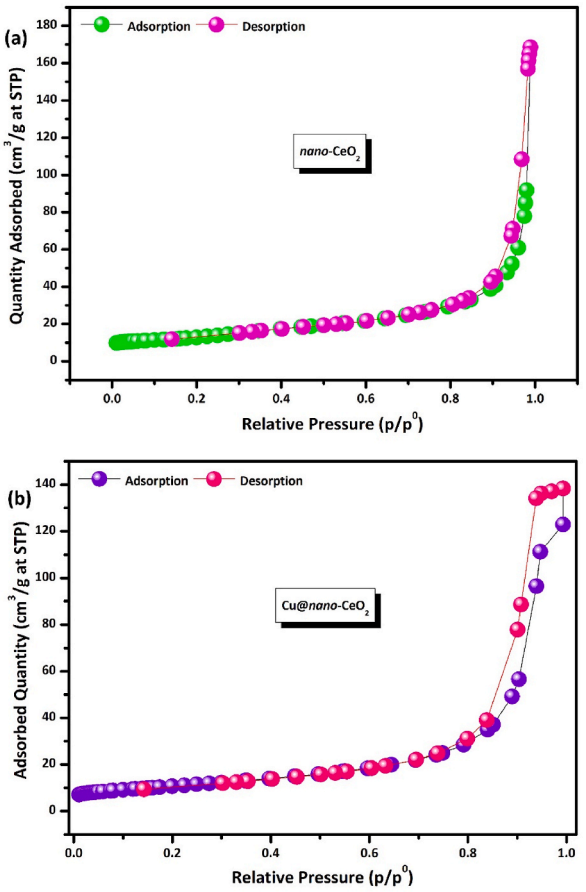

Fig. 4. N_2 Adsorption desorption isotherms of *nano*-CeO_2 (a) and Cu@*nano*-CeO_2 (b) samples.

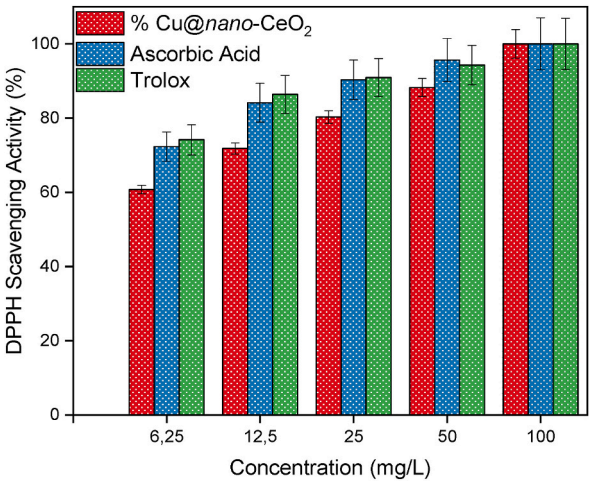

Fig. 5. DPPH scavenging activity of Cu@*nano*-CeO_2

control one.

$$\text{Microbial cell viability } (\%) = \left(A_{control} - A_{sample} \ / \ A_{control}\right) \text{ x } 100$$

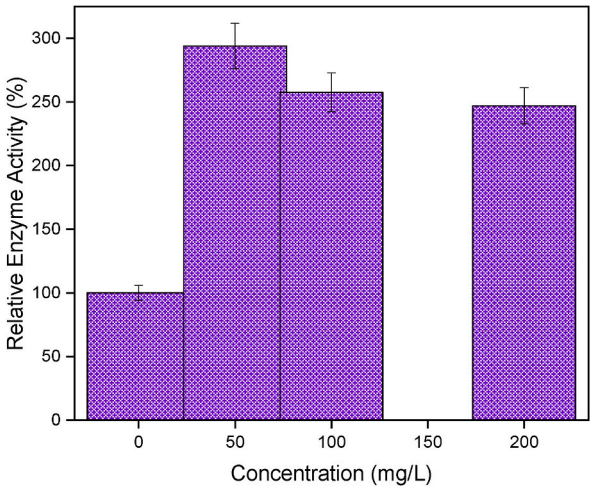

Fig. 6. The effect of Cu@*nano*-CeO_2 concentrations on α-amylase activity.

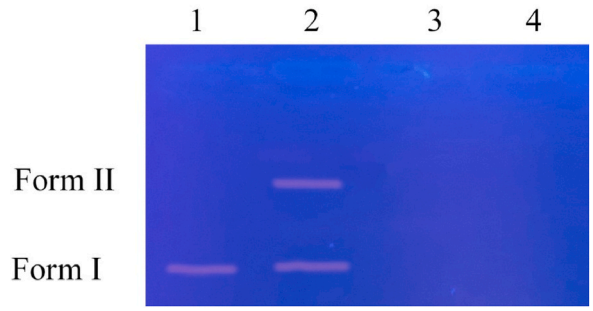

Fig. 7. DNA cleavage activity of Cu@*nano*-CeO_2 nanostructure. Lane 1, pBR 322 DNA; Lane 2, pBR 322 DNA +50 mg/L Cu@*nano*-CeO_2; Lane 3, pBR 322 DNA +100 mg/L of Cu@*nano*-CeO_2; Lane 4, pBR 322 DNA +200 mg/L of Cu@*nano*-CeO_2.

Table 1
Antimicrobial activity of Cu@*nano*-CeO_2

Microorganisms	MICs (mg/L)
E. coli	64
P. aeruginosa	128
L. pneumophila* subsp. *pneumophila	128
E. hirae	16
E. fecalis	16
S. aureus	32
C. tropicalis	256
C. albicans	256

2.10. Biofilm inhibition activity of Cu@nano-CeO_2

P. aeruginosa and *S. aureus* overnight culture were diluted in fresh media and adjusted to 1×10^8 CFU/mL. These bacterial suspensions were added to a 48-well plate containing Cu-doped CeO_2 concentrations of 12.5, 25, and 50 mg/L. This plate was then incubated at 37 °C for 72 h. To remove planktonic cells, the contents were evacuated and the wells were cleaned three times with distilled water. The bacterial biofilm was stained with 0.1 % crystal violet for 30 min. The surplus dye was washed away with water, then absolute ethanol was used to dissolve the biofilm. The absorbance was measured at 595 nm. The biofilm inhibition was calculated using the formula below.

$$\text{Biofilm Inhibition } (\%) = \left(\text{Abs}_{(\text{control})} - \text{Abs}_{(\text{sample})} \,/\, \text{Abs}_{(\text{control})}\right) \times 100$$

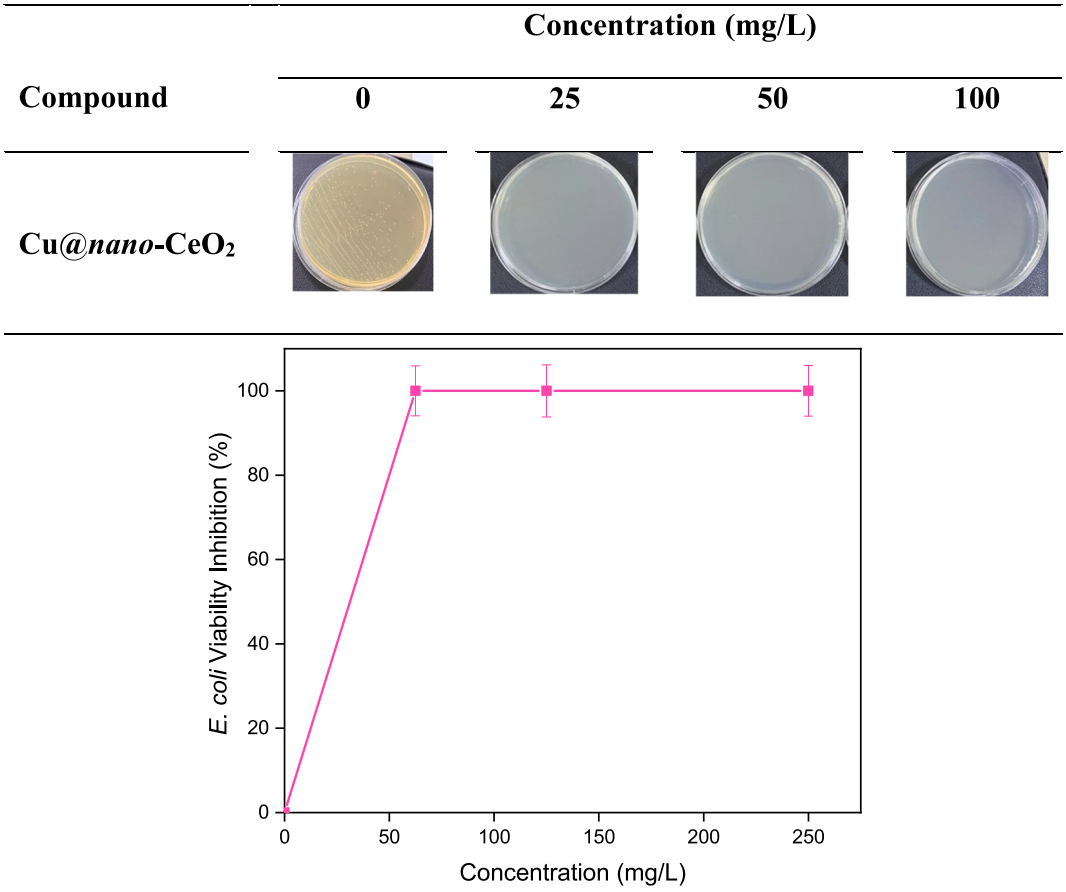

Fig. 8. Microbial cell viability inhibition of Cu@*nano*-CeO_2

2.11. Application of polyethersulfone (PES) membrane coated with Cu@nano-CeO_2 for E. coli removal and its solid surface antimicrobial activity

The application of polyethersulfone (PES) membrane coated with Cu@*nano*-CeO_2 for *E. coli* removal and its solid surface antimicrobial activity was evaluated according to our previous work [36].

3. Results and discussion

3.1. Characterization of Cu@nano-CeO_2 nanostructure

The structural and morphological properties of the Cu@*nano*-CeO_2 material were evaluated through ICP-OES, XRD, XPS, SEM, and BET analyses. In the initial stage, ICP-OES analysis was employed to assess the distribution of Cu metal content on CeO_2 NPs, revealing a Cu content of 1.82 ± 0.06 wt%. It is noteworthy that the designed theoretical metal content of the Cu@*nano*-CeO_2 material was intended to be 2.0 wt% Cu. In the XRD pattern provided in Fig. 1 for determining the crystallinity of *nano*-CeO_2 and Cu@*nano*-CeO_2 samples, it is evaluated that the observed Bragg peaks at 28.5°, 33.2°, 47.5°, 56.3°, 59.1°, 69.5°, 76.7°, 79.2° and 88.6° correspond to the (111), (200), (220), (311), (222), (400), (331), (420), and (422) planes, respectively. When the XRD pattern of *nano*-CeO_2 is compared with the standard diffraction pattern of cerium oxide (JCPDS card number 34–0394), it is observed that the crystal structure of the present cerium oxide sample is cubic fluorite structure [15,33,37,38]. It is also observed that the XRD pattern of Cu@*nano*-CeO_2 completely overlaps with that of *nano*-CeO_2. According to the ICP-OES analysis, no signal for Cu is observed in the XRD pattern due to low Cu doping on the surface of *nano*-CeO_2. However, it is also concluded that there is no alteration or collapse in the crystal structure of *nano*-CeO_2, which is the host material in the nanoparticle production process.

XPS offers additional insights into the oxidation state of copper and the surface composition of the resulting Cu@*nano*-CeO_2. In Fig. 2 (a), the survey scan XPS spectrum of the Cu@*nano*-CeO_2 sample illustrates the presence of *nano*-CeO_2 elements (Ce and O) along with copper (Cu). Fig. 2 (b) displays the high-resolution Cu 2p XPS spectrum of the Cu@*nano*-CeO_2 sample, which has a loading of 1.82 ± 0.06 wt% Cu, along with its deconvolution. The deconvolution of the high-resolution Cu 2p XPS spectrum reveals two distinct peaks at 933.2 eV (Cu $2p_{3/2}$) and 942.69 eV (Cu $2p_{1/2}$), indicating metallic Cu (0), as supported by previous studies [34,39]. Furthermore,

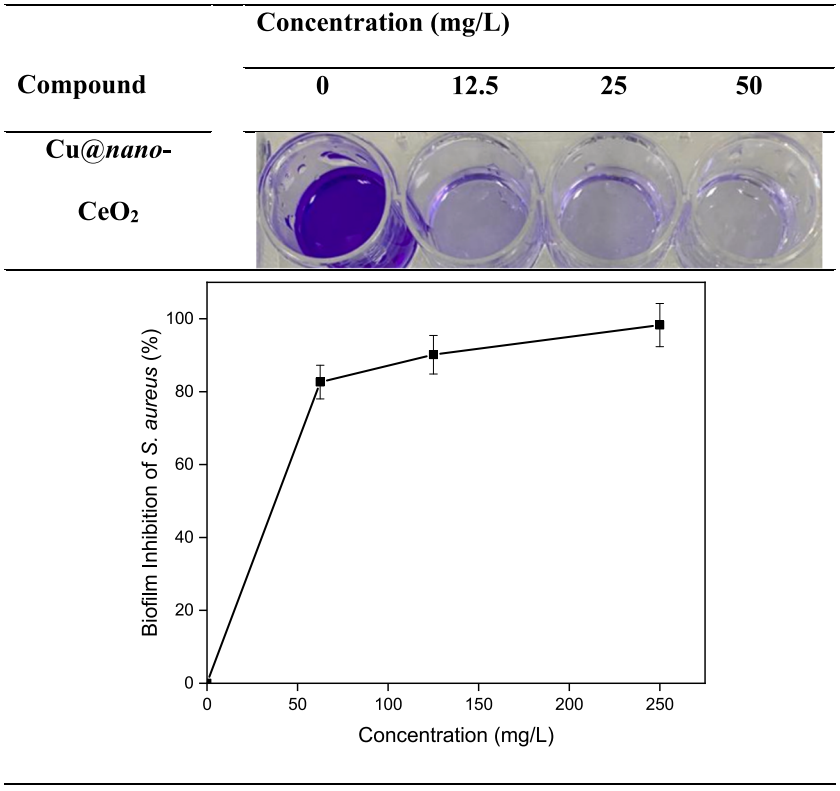

Fig. 9. Biofilm inhibition of *S. Aureus*.

peaks observed at 953.21 eV suggest the presence of the CuO phase, likely resulting from the surface oxidation of Cu (0) NPs during the XPS sampling procedure [22,40]. Fig. 2 (c) reveals the high-resolution Ce 3d spectra consisting of spin-orbit pairs Ce $3d_{5/2}$ (883.21 eV) and Ce $3d_{3/2}$ (900.20 eV). These binding energies are well attributed to the predominant Ce^{4+} and Ce^{3+} oxidation states in CeO_2 nanoparticles. In the deconvoluted O 1s spectrum (Fig. 2 (d)), the two main binding energies observed at 528.21 eV and ~528.76 eV can be associated with lattice oxygen ions (O_{lat}) and surface-adsorbed oxygen ions (O_{ads}), respectively [41,42].

The morphological analysis of the Cu@*nano*-CeO_2 nanostructure was conducted using SEM. In Fig. 3(a–c), SEM images of the samples are presented alongside their corresponding EDX spectrum. As depicted in Fig. 3(a and b), Cu NPs exhibit a nearly uniform distribution on the surface of *nano*-CeO_2. Consistent with expectations, the EDX spectra of *nano*-CeO_2 reveal the presence of Ce and O elements alongside carbon, likely originating from the carbon tape used during sample preparation. Additionally, the homogeneous distribution of Cu, Ce, and O observed in the SEM-elemental mapping of Cu@*nano*-CeO_2 (Fig. 3 (d)) further confirms the presence of Cu (0) NPs on the *nano*-CeO_2 support. It is also important to note that the Au signals originate from the SEM sample carrier.

Fig. 4(a–b) displays the N_2 adsorption-desorption isotherms for both *nano*-CeO_2 and Cu@*nano*-CeO_2 samples, with BET analysis conducted to assess their surface area and porosity. The isotherms for each sample exhibit type IV and H3 hysteresis loops, in line with the IUPAC classification characteristic of mesoporous materials [43,44]. The BET surface area of *nano*-CeO_2 and Cu@*nano*-CeO_2 was determined as 46.02 m^2/g and 38.18 m^2/g, respectively, based on the linear portion of the BET plots. The observed decrease in pore volume and BET surface area upon transitioning from *nano*-CeO_2 to Cu@*nano*-CeO_2 can be attributed to the blockage of *nano*-CeO_2 pores by Cu (0) NPs, as evidenced by SEM analysis (as discussed earlier).

3.2. *Free radical scavenging activity (FRSA) of Cu@nano-CeO_2*

The antioxidant assays assess a sample's antioxidant potential based on its ability to donate electrons or hydrogen atoms [45]. The antioxidant potential of Cu@*nano*-CeO_2 was investigated. The obtained results were evaluated to compare with ascorbic acid and Trolox (Fig. 5). At a concentration of 6.25 mg/L, FRSA of Cu@*nano*-CeO_2, ascorbic acid, and Trolox was 60.73, 72.31, and 74.16 %, respectively. When the concentration was increased up to 100 mg/L, FRSAs was elevated 100 % by Cu@*nano*-CeO_2. It is clearly seen that Cu@*nano*-CeO_2 has significant antioxidant potential depending on the concentration. This antioxidant capability could be attributed to the presence of functional groups on the surface of nanoparticles or to the nanoparticle itself [46]. Because of the two oxidation states of Ce^{+3} and Ce^{+4}, the free radical scavenging activity of Cu@*nano*-CeO_2 is highly connected to the redox potential [47]. Jan et al. synthesized CeO_2 NPs using a green chemistry approach. They also investigated the antioxidant potential of CeO_2 NPs and reported that CeO_2 NPs showed significant in vitro antioxidant abilities [48]. Butt et al. produced CeO_2 NPs via biogenic synthesis.

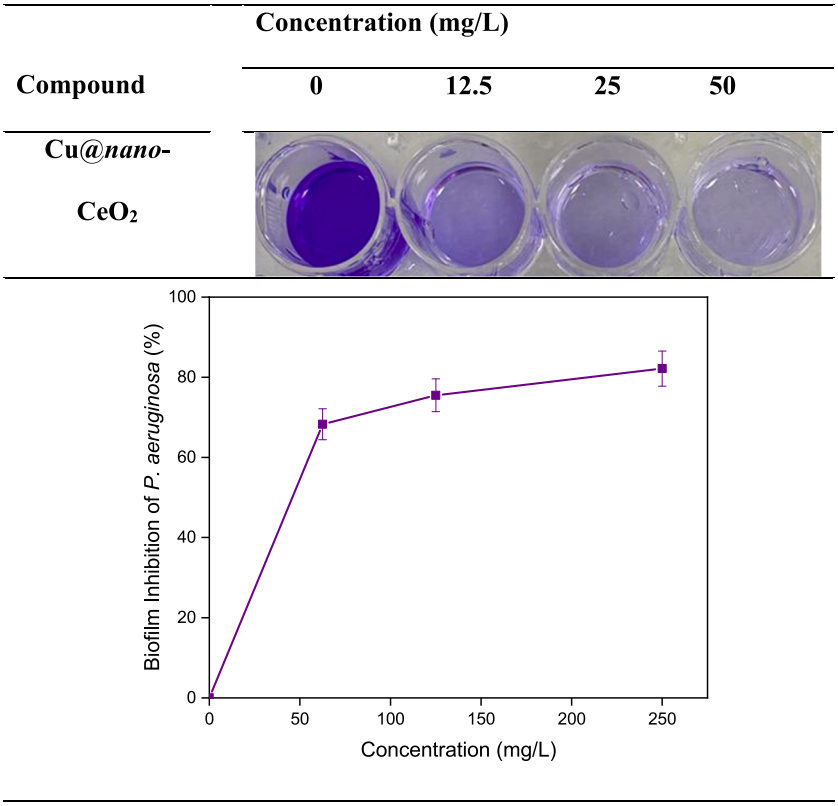

Fig. 10. Biofilm inhibition of *P. aeruginosa*.

They reported that CeO_2 NPs exhibited moderate FRSA (40.6 ± 1 %) [49]. From our findings, we can conclude that the Cu@*nano*-CeO_2 has a strong anti-radical effect.

3.3. Enhancement effect of Cu@nano-CeO_2 on α-amylase

The influence of Cu@*nano*-CeO_2 on the α-amylase enzyme was investigated using the DNS method. As seen in Fig. 6, in a concentration-dependent manner, the tested sample activated α-amylase activity. When the concentration was 50, 100, and 200 mg/L, the promoted ratio reached 293.9, 257.6, and 247.0 %, respectively. Cu NPs in the tested sample structure at a lower concentration significantly enhanced the enzyme activity but gradually decreased with increasing Cu@*nano*-CeO_2 concentration. Similar findings have been reported in the literature for different nanoparticles. Abdel-Nasser et al. reported that the α-amylase activity was increased gradually with increasing the Au and Ag-NPs, but after a certain concentration, enzyme activity was decreased gradually [50]. Saware et al. found that at low concentrations, Ag NPs stimulate α-amylase activity while inhibiting it at high concentrations [51]. According to the data we obtained, amylase activity increased approximately 3 times at 50 mg/L. In this context, Cu@*nano*-CeO_2 can be used to increase α-amylase activity in various industries where α-amylase is used.

3.4. DNA cleavage activity of Cu@nano-CeO_2

To investigate the DNA nuclease activity of Cu@*nano*-CeO_2, agarose gel electrophoresis tests were carried out using pBR322 plasmid DNA, as described in the experimental section. When plasmid DNA is treated with a substance capable of breaking the DNA strand, it acts like a nuclease and 'scissors' the DNA's supercoiled circular Form I at specific positions to give nicked circular Form II and linear Form III. This was investigated by treating pBR322 plasmid with Cu@*nano*-CeO_2 at 50, 100, and 200 mg/L concentrations. The electrophoresis image is presented in Fig. 7. At 50 mg/L concentration, one strand was cleaved, the supercoiled form I relaxed and relatively slower-moving form II was produced (Lane 2). At 100 and 200 mg/L concentrations of the sample, it was observed that the nuclease activity of Cu@*nano*-CeO_2 was very effective (Lanes 3 and 4) and the complete cleavage of the DNA strand was obtained. In general, 3 different types of DNA cleavage mechanisms can be distinguished, DNA photochemical cleavage, oxidative cleavage, and also hydrolysis, although the first two mechanisms are quite closely related. Probably, Cu@*nano*-CeO_2 compounds caused DNA cleavage via DNA hydrolysis mechanism. The widely accepted mechanism of the DNA hydrolysis reaction is a nucleophilic attack on the DNA phosphate backbone to form a five-coordinate intermediate that can be stabilized by a catalyst. Subsequent cleavage of the 3′-PO or 5′-PO results in strand scission [52]. Consequently, the nuclease experiments applied using agarose gel clearly suggest that the

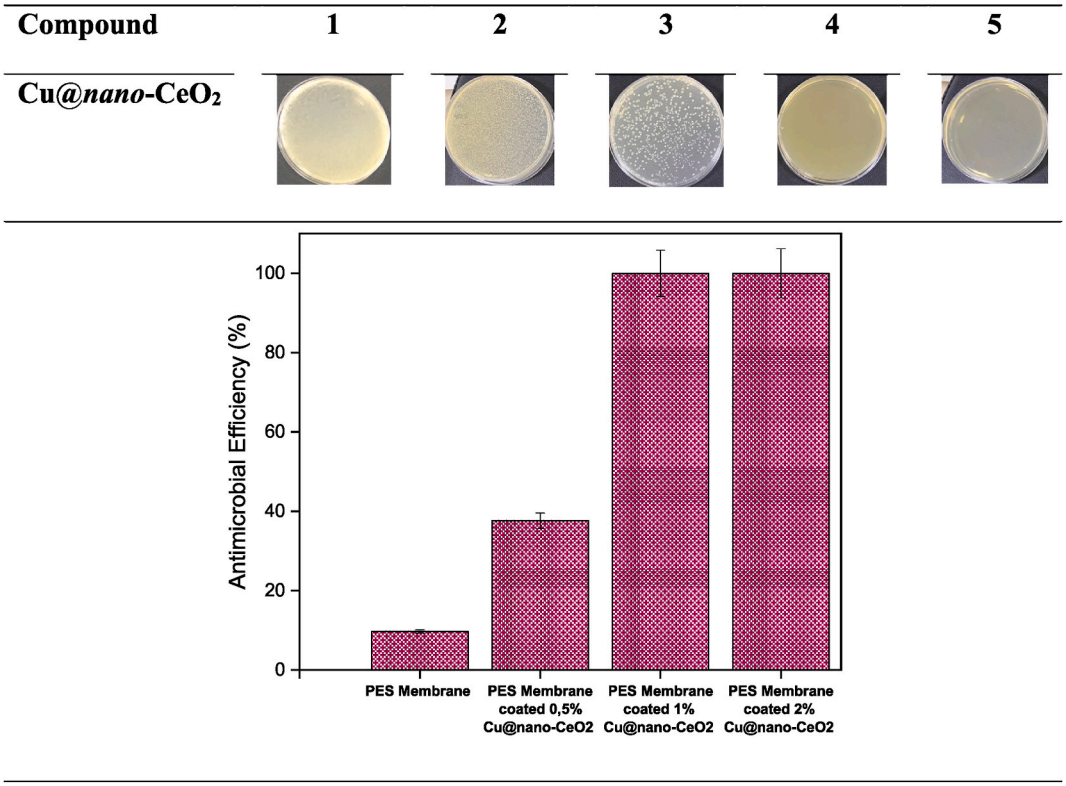

Fig. 11. Performing of PES membrane surface coated with Cu@*nano*-CeO_2 for removal of *E. coli*. (1: Control; 2: PES Membrane; 3: 0.5 % Cu@*nano*-CeO_2 doped PES Membrane; 4: 1 % Cu@*nano*-CeO_2 doped PES Membrane; 5: 2 % Cu@*nano*-CeO_2 doped PES Membrane.

Cu@*nano*-CeO_2 exhibits an effective DNA nuclease activity and Cu@*nano*-CeO_2 can be utilized for anti-cancer and antimicrobial studies.

3.5. Antimicrobial activity of Cu@nano-CeO_2

An antimicrobial assay was performed to determine MIC values of Cu@*nano*-CeO_2 against different microbial strains. MIC values of Cu@*nano*-CeO_2 were 16 mg/L against *E. hirae* and *E. feacalis*, 32 mg/L against *S. aureus*, 64 mg/L against *E. coli*, 128 mg/L against *P. aeruginosa* and *L. pneumophila* subsp. *Pneumophila,* 256 mg/L against *C. tropicalis* and *C. Albicans* (Table 1). The antibacterial mechanism is still unclear, but it is likely proposed as follows. The negatively charged cell walls of both Gram-positive and Gram-negative bacteria electrostatically attract the positively charged Cu@*nano*-CeO_2. Zeta potential (Malvern Zeta Sizer Nano ZS) value of Cu@*nano*-CeO_2 was measured as 2.06 ± 0.13 mV. This interaction cause the release Ce^{3+}, Ce^{4+} and Cu^{+} ions. These ions induce the production of reactive oxygen species (ROS) on the bacterial cell membrane. ROS generation hinders the antioxidant defense system and damages the cell membrane mechanically [49,53]. Pandiyan et al. fabricated SrO/CeO_2 nanostructure using a green synthesis approach. Biofabricated SrO/CeO_2 NPs showed important antibacterial activity, especially against *S. aureus* (G+) than *E. coli* (G−) bacteria [54]. Maleki et al. synthesized Ag-doped CeO_2 NPs using Salvia seeds extract. They reported that Ag-doped CeO_2 NPs had excellent antibacterial activity against *S. aureus* and *P. Aeruginosa* [53]. The data obtained after antimicrobial activity experiments show that the strong inhibitory effect of Cu@*nano*-CeO_2 is supported by the literature.

3.6. Microbial cell viability inhibition of Cu@nano-CeO_2

The inhibition activity of Cu@*nano*-CeO_2 to *E. coli* cell viability was evaluated at different concentrations (25, 50, and 100 mg/L). After 2 h of contact with Cu@*nano*-CeO_2, cell viability was determined. The results are presented in Fig. 8. The results indicated that the cell viability of *E. coli* was strongly inhibited at all tested concentrations by Cu@*nano*-CeO_2. A bacterium's membrane fluidity is essential to maintain a normal cellular structure, cell division, and diffusion functions, and resist environmental stresses [55]. After 2 h of contact between *E. coli* cells and Cu@*nano*-CeO_2, membrane fluidity may decrease so this was related to the decrease in cell viability. After NPs come into contact with the cell membrane, they enter the cell through interactions such as electrostatic attraction, van der Waals forces, hydrophobic interactions, and receptor–ligand, affecting the shape and function of the cell membrane. Then, NPs interact with the basic components of the microorganism cell, such as lysosomes, DNA, enzymes, and ribosomes, leading to heterogeneous changes, oxidative stress, electrolyte imbalances, changes in cell membrane permeability, enzyme inhibition, gene expression changes,

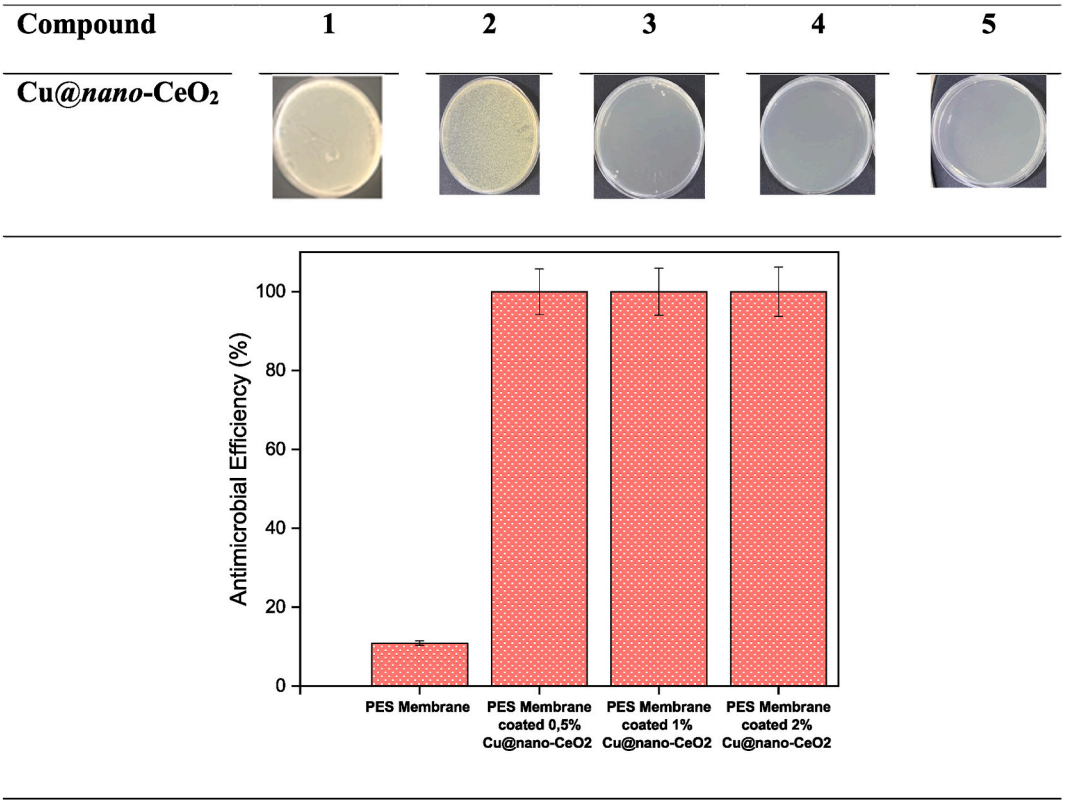

Fig. 12. Performing of PES membrane coated with Cu@*nano*-CeO_2 for *E. coli* filtration process. (1: Control; 2: PES Membrane; 3: 0.5 % Cu@*nano*-CeO_2 doped PES Membrane; 4: 1 % Cu@*nano*-CeO_2 doped PES Membrane; 5: 2 % Cu@*nano*-CeO_2 doped PES Membrane.

and protein deactivation Wang et al. (2017) [56]. Cu@*nano*-CeO_2 interacts strongly with membrane lipids, which may result in Cu@*nano*-CeO_2 penetration into cell membranes, oxidation of membrane phospholipids by Ce^{4+}, and consequently membrane instability and fluidity reduction [57]. As a result, Cu@*nano*-CeO_2 can be used for effective microbial disinfection.

3.7. Evaluation of antibiofilm activity of Cu@nano-CeO_2

Biofilms are classified as self-produced structures by microbes, mainly composed of extracellular polymeric substances such as proteins, carbohydrates, and extracellular DNA. These extracellular polymeric substances enable biofilm stability and aid microbe adhesion to biotic and abiotic surfaces [58,59]. Moreover, the bacteria growing in the biofilms have an inherent resistance to chemical therapeutic drugs like antibiotics. As a result, attacking biofilms is regarded as a novel method of reducing bacterial infections. Cu@*nano*-CeO_2 was tested for anti-biofilm effects against two well-known biofilm-forming bacteria, *S. aureus*, and *P. aeruginosa*. Cu@*nano*-CeO_2 exhibited a dose-dependent effect on *S. aureus* and *P. aeruginosa* biofilms, as seen in Figs. 9 and **10**. At 12.5, 25, and 50 mg/L concentrations of Cu@*nano*-CeO_2, biofilm formation of *S. aureus* and *P. aeruginosa* were inhibited at 82.63, 90.13, and 98.27 % and 68.26, 75.49, and 82.14 % respectively, when compared with control. In earlier studies, Altaf et al. reported that biogenic synthesized CeO_2 NPs had 70 % inhibition of *S. aureus* biofilm [60], and Naidi et al. reported 65 % destruction of bacterial biofilm with green synthesized Sn-doped CeO_2 NPs [61]. Iqbal et al. reported that biosynthesized CeO_2-graphene oxide nanocomposites exhibited 82 and 60 % inhibition of *P. aeruginosa* and *S. aureus* biofilm, respectively [62]. Our findings demonstrated that Cu@*nano*-CeO_2 inhibited biofilm production more effectively while also being disruptive to mature biofilm.

3.8. Application of polyethersulfone (PES) membrane coated with Cu@nano-CeO_2 for E. coli removal and its solid surface antimicrobial activity

In order to determine wastewater treatment potential, the inhibition activity of PES/Cu@*nano*-CeO_2 membrane to *E. coli* cell viability was also investigated. The inhibition activities of bare PES membrane, PES/Cu@*nano*-CeO_2 0.50 wt% membrane, PES/Cu-doped CeO_2 1.0 wt% membrane, and PES/Cu-doped CeO_2 2.0 wt% membrane were 9.69 %, 37.63 %, 100.0 %, and 100.0 %, respectively (Fig. 11). Moreover, *E. coli* removal efficiency of the PES/Cu@*nano*-CeO_2 membrane during the wastewater treatment process was tested. For this purpose, the filtrates obtained using the membranes given above were studied for *E. coli* removal. Obtained results are given in Fig. 12. While bare PES membrane exhibited 10.87 % inhibition activity, PES/Cu@*nano*-CeO_2 0.50, 1.0, and 2.0 wt

% membranes exhibited 100.0 % inhibition activity. Our findings demonstrated that the Cu@*nano*-CeO_2 blended membrane has the potential to improve treatment efficiency and water supply by being used in water and wastewater treatment procedures.

4. Conclusion

The Cu@*nano*-CeO_2 nanostructure showed highly potent antioxidant activity as 100 %. It activated the α-amylase enzyme in a concentration-dependent manner and α-amylase enzyme activity was enhanced 293.94 % at 50 mg/L. After nuclease activity experiments using agarose gel, it was determined that Cu@*nano*-CeO_2 nanostructure exhibited an effective DNA nuclease activity. The Cu@*nano*-CeO_2 nanostructure provided highly promising antimicrobial properties and inhibited biofilm formation against *S. aureus* and *P. aeruginosa*. The highest biofilm inhibition was determined as 98.3 % against *S. aureus*. Moreover, it was determined that the Cu@*nano*-CeO_2 nanostructure blended polyethersulfone membrane strongly inhibited *E. coli* viability (100 %) after it was applied to the wastewater treatment system.

CRediT authorship contribution statement

Lokman Şener: Methodology, Investigation, Formal analysis, Data curation. **Sadin Özdemir:** Methodology, Investigation, Formal analysis, Conceptualization. **M. Serkan Yalçın:** Methodology, Investigation, Formal analysis, Data curation, Conceptualization. **Mehmet Gülcan:** Writing – review & editing, Writing – original draft, Supervision, Data curation, Conceptualization. **Nadir Dizge:** Writing – review & editing, Writing – original draft, Supervision, Formal analysis, Data curation.

Data availability statement

Data will be made available on request.

Declaration of competing interest

The authors declare the following financial interests/personal relationships which may be considered as potential competing interests: Mehmet Gülcan is an ABM of the Heliyon journal. If there are other authors, they declare that they have no known competing financial interests or personal relationships that could have appeared to influence the work reported in this paper.

References

[1] T. Montini, M. Melchionna, M. Monai, P. Fornasiero, Fundamentals and catalytic applications of CeO_2-based materials, Chem. Rev. 116 (2016) 5987–6041, https://doi.org/10.1021/acs.chemrev.5b00603.
[2] H. Yan, N. Zhang, D. Wang, Highly efficient CeO_2-supported noble-metal catalysts: from single atoms to nanoclusters, Chem Catal. 2 (2022) 1594–1623, https://doi.org/10.1016/j.checat.2022.05.001.
[3] J. Gagnon, K.M. Fromm, Toxicity and protective effects of cerium oxide nanoparticles (Nanoceria) depending on their preparation method, particle size, cell type, and exposure route, Eur. J. Inorg. Chem. 27 (2015) 4510–4517, https://doi.org/10.1002/ejic.201500643.
[4] Z. Tian, J. Li, Z. Zhang, W. Gao, X. Zhou, Y. Qu, Highly sensitive and robust peroxidase-like activity of porous nanorods of ceria and their application for breast cancer detection, Biomater 59 (2015) 116–124, https://doi.org/10.1016/j.biomaterials.2015.04.039.
[5] X. Beaudoux, M. Virot, T. Chave, G. Durand, G. Leturcq, S.I. Nikitenko, Vitamin C boosts ceria-based catalyst recycling, Green Chem. 18 (2016) 3656–3668, https://doi.org/10.1039/C6GC00434B.
[6] M.B. Gawande, V.D.B. Bonifacio, R.S. Varma, I.D. Nogueira, N. Bundaleski, C.A.A. Ghumman, O.M.N.D. Teodoro, P.S. Branco, Magnetically recyclable magnetite-ceria (Nanocat-Fe-Ce) nanocatalyst – applications in multicomponent reactions under benign conditions, Green Chem. 15 (2013) 1226–1231, https://doi.org/10.1039/C3GC40375K.
[7] C. Xu, X. Qu, Cerium oxide nanoparticle: a remarkably versatile rare earth nanomaterial for biological applications, NPG Asia Mater. 6 (2014) e90, https://doi.org/10.1038/am.2013.88.
[8] F. Charbgoo, M.B. Ahmad, M. Darroudi, Cerium oxide nanoparticles: green synthesis and biological applications, Int. J. Nanomed. 12 (2017) 1401–1413, https://doi.org/10.2147/IJN.S124855.
[9] S. Das, J.M. Dowding, K.E. Klump, J.F. McGinnis, W. Self, S. Seal, Cerium oxide nanoparticles: applications and prospects in nanomedicine, Nanomed, (Lond) 8 (2013) 1483–1508, https://doi.org/10.2217/nnm.13.133.
[10] S. Deshpande, S. Patil, S.V. Kuchibhatla, S. Seal, Size dependency variation in lattice parameter and valency states in nanocrystalline cerium oxide, Appl. Phys. Lett. 87 (2005) 133113, https://doi.org/10.1063/1.2061873.
[11] I. Celardo, J.Z. Pedersen, E. Traversa, L. Ghibelli, Pharmacological potential of cerium oxide nanoparticles, Nanoscale 3 (2011) 1411–1420, https://doi.org/10.1039/C0NR00875C.
[12] M. Li, P. Shi, C. Xu, J. Ren, X. Qu, Cerium oxide caged metal chelator: anti-aggregation and anti-oxidation integrated H_2O_2-responsive controlled drug release for potential Alzheimer's disease treatment, Chem. Sci. 4 (2013) 2536–2542, https://doi.org/10.1039/C3SC50697E.
[13] C. Xu, Y. Lin, J. Wang, Nanoceria-triggered synergetic drug release based on CeO_2-capped mesoporous silica host–guest interactions and switchable enzymatic activity and cellular effects of CeO_2, Adv. Healthc. Mater. 2 (2013) 1591–1599, https://doi.org/10.1002/adhm.201200464.
[14] K.R.B. Singh, V. Nayak, T. Sarkar, R.P. Singh, Cerium oxide nanoparticles: properties, biosynthesis and biomedical application, RSC Adv. 10 (2020) 27194, https://doi.org/10.1039/D0RA04736H.
[15] P.P. Tumkur, N.K. Gunasekaran, B.R. Lamani, N.N. Bayon, K. Prabhakaran, J.C. Hall, G.T. Ramesh, Cerium oxide nanoparticles: synthesis and characterization for biosafe applications, Nanomanufacturing 1 (2021) 176–189, https://doi.org/10.3390/nanomanufacturing1030013.
[16] H. Nosrati, M. Heydari, M. Khodaei, Cerium oxide nanoparticles: synthesis methods and applications in wound healing, Mater. Today Bio. 23 (2023) 100823, https://doi.org/10.1016/j.mtbio.2023.100823.
[17] A. Younis, D. Chu, S. Li, A. Younis, D. Chu, S. Li, Cerium oxide nanostructures and their applications, in: Functionalized Nanomaterials, 2016. IntechOpen: London, UK, https://www.intechopen.com/chapters/52860. (Accessed 24 March 2024).
[18] K. Akhtar, S.A. Khan, S.B. Khan, A.M. Asiri, Scanning electron microscopy: principle and applications in nanomaterials characterization, in: Handbook of Materials Characterization, Springer, Basingstoke, UK, 2018. ISBN 9783319929552.

[19] L. Dong, M.M. Craig, D. Khang, C. Chen, Applications of nanomaterials in biology and medicine, J. Nanotechnol. 2012 (2012) 1–2, https://doi.org/10.1155/2012/816184.

[20] B.L. Cushing, L. Kolesnichenko, C.J. Connor, Recent advances in the liquid-phase syntheses of inorganic nanoparticles, Chem. Rev. 104 (2004) 3893–3996, https://doi.org/10.1021/cr030027b.

[21] M. Zahmakiran, S. Ozkar, Metal nanoparticles in liquid phase catalysis; from recent advances to future goals, Nanoscale 3 (2011) 3462–3481, https://doi.org/10.1039/C1NR10201J.

[22] I.B. Baguc, I.E. Ertas, M. Yurderi, A. Bulut, M. Zahmakiran, M. Kaya, Nanocrystalline metal organic framework (MIL-101) stabilized copper nanoparticles: highly efficient nanocatalyst for the hydrolytic dehydrogenation of methylamine borane, Inorg. Chim. Acta. 483 (2018) 431–439, https://doi.org/10.1016/j.ica.2018.08.056.

[23] R.A. Al-Juboori, T. Yusaf, Biofouling in RO system: mechanisms, monitoring and controlling, Desalination 302 (2012) 1–23.

[24] J.M. Ochando-Pulido, M. Stoller, L. Di Palma, A. Martínez-Ferez, On the optimization of a flocculation process as fouling inhibiting pretreatment on an ultrafiltration membrane during olive mill effluents treatment, Desalination 393 (2016) 151–158.

[25] S. Jiang, Y. Li, B.P. Ladewig, A review of reverse osmosis membrane fouling and control strategies, Sci. Total Environ. 595 (2017) 567–583.

[26] D. Rana, T. Matsuura, Surface modifications for antifouling membranes, Chem. Rev. 110 (4) (2010) 2448–2471.

[27] D.S. Wavhal, E.R. Fisher, Membrane surface modification by plasmainduced polymerization of acrylamide for improved surface properties and reduced protein fouling, Langmuir 19 (1) (2003) 79–85.

[28] C. Zhang, F. Yang, W. Wang, B. Chen, Preparation and characterization of hydrophilic modification of polypropylene non-woven fabric by dip-coating PVA (polyvinyl alcohol), Sep. Purif. Technol. 61 (3) (2008) 276–286.

[29] L. Zhu, H. Dong, X. Wei, Z. Yi, B. Zhu, Y. Xu, Tethering hydrophilic polymer brushes onto PPESK membranes via surface-initiated atom transfer radical polymerization, J. Membr. Sci. 320 (1–2) (2008) 407–415.

[30] Y. Zhou, S. Yu, C. Gao, X. Feng, Surface modification of thin film composite polyamide membranes by electrostatic self deposition of polycations for improved fouling resistance, Sep. Purif. Technol. 66 (2) (2009) 287–294.

[31] M. Zhou, H. Liu, J. Kilduff, R. Langer, D. Anderson, G. Belfort, Highthroughput membrane surface modification to control NOM fouling, Environ. Sci. Technol. 43 (10) (2009) 3865–3871.

[32] Q. Yang, B. Mi, Nanomaterials for membrane fouling control: accomplishments and challenges, Adv. Chronic Kidney Dis. 20 (6) (2013) 536–555.

[33] Y. Karatas, M. Gülcan, F. Sen, Catalytic methanolysis and hydrolysis of hydrazine-borane with monodisperse Ru NPs@*nano*-CeO_2 catalyst for hydrogen generation at room temperature, Int. J. Hydrogen Energy 44 (2019) 13432–13442, https://doi.org/10.1016/j.ijhydene.2019.04.012.

[34] R. Yıldırım, Y. Karatas, U.B. Demirci, M. Gülcan, Fabrication and characterization of copper nanoparticles anchored on sulfonated reduced graphene oxide as effective catalyst for the reduction of Thioflavine-T cationic dye in aqueous medium, Mater. Chem. Phys. 275 (2022) 125212, https://doi.org/10.1016/j.matchemphys.2021.125212.

[35] M.S. Blois, Antioxidant determinations by the use of a stable free radical, Nature 181 (1958) 1199–1200, https://doi.org/10.1038/1811199a0.

[36] S. Gonca, Z. Isik, S. Özdemir, H. Arslan, N. Dizge, The surface modification of ultrafiltration membrane with silver nanoparticles using *Verbascum thapsus* leaf extract using green synthesis phenomena, Surf. Interfaces 26 (2021) 101291, https://doi.org/10.1016/j.surfin.2021.101291.

[37] M. Chelliah, J.B.B. Rayappan, U.M. Krishnan, Synthesis and characterization of cerium oxide nanoparticles by hydroxide mediated approach, J. Appl. Sci. 12 (2012) 1734–1737. https://scialert.net/abstract/?doi=jas.2012.1734.1737.

[38] K. Deori, D. Gupta, B. Saha, S.K. Awasthi, S. Deka, Introducing nanocrystalline CeO_2 as heterogeneous environmental friendly catalyst for the aerobic oxidation of para-xylene to terephthalic acid in water, J. Mater. Chem. A 1 (2013) 7091–7099, https://doi.org/10.1039/C3TA01590D.

[39] Y.-F. Li, F.-X. Dong, Y. Chen, X.-L. Zhang, L. Wang, Y.-G. Bi, Z.-N. Tian, Y.-F. Liu, J. Feng, H.-B. Sun, As-grown graphene/copper nanoparticles hybrid nanostructures for enhanced intensity and stability of surface plasmon resonance, Sci. Rep. 6 (2016) 37190, https://doi.org/10.1038/srep37190.

[40] A. Bulut, M. Yurderi, I.E. Ertas, M. Celebi, M. Zahmakiran, M. Kaya, Pd-MnOx nanoparticles dispersed on amine-grafted silica: highly efficient nanocatalyst for hydrogen production from additive-free dehydrogenation of formic acid under mild conditions, Appl. Catal. B Env. 164 (2015) 324–333, https://doi.org/10.1016/j.apcatb.2014.09.041.

[41] K.I. Maslakov, Y.A. Teterin, A.J. Popel, A.Y. Teterin, K.E. Ivanov, S.N. Kalmykov, V.G. Petrov, P.K. Petrov, I. Farnan, XPS study of ion irradiated and unirradiated CeO_2 bulk and thin film samples, Appl. Surf. Sci. 448 (2018) 154–162, https://doi.org/10.1016/j.apsusc.2018.04.077.

[42] G. Murugadoss, D.D. Kumar, M.R. Kumar, N. Venkatesh, P. Sakthivel, Silver decorated CeO_2 nanoparticles for rapid photocatalytic degradation of textile rose bengal dye, Sci. Rep. 11 (2021) 1080, https://doi.org/10.1038/s41598-020-79993-6.

[43] T.V. Tuyen, N.K. Chi, D.T. Tien, N. Tu, N.V. Quang, P.T.L. Huong, Carbon encapsulated $MnFe_2O_4$ nanoparticles: effects of carbon on structure, magnetic properties and Cr(VI) removal efficiency, Appl. Phys. A 126 (2020) 577, https://doi.org/10.1007/s00339-020-03760-7.

[44] Y. Karataş, A. Zengin, M. Gülcan, Pd-doped flower like magnetic $MnFe_2O_4$ spinel ferrit nanoparticles: synthesis, structural characterization and catalytic performance in the hydrazine-borane methanolysis, J. Energy Inst. 110 (2023) 101360, https://doi.org/10.1016/j.joei.2023.101360.

[45] Y. El Atki, I. Aouam, F. El kamari, A. Taroq, B. Lyoussi, M. Taleb, A. Abdellaoui, Total phenolic and flavonoid contents and antioxidant activities of extracts from *Teucrium polium* growing wild in Morocco, Mater. Today Proc. 13 (2019) 777–783, https://doi.org/10.1016/j.matpr.2019.04.040.

[46] S. Naz, S.T. Kazmi, M. Zia, CeO_2 nanoparticles synthesized through green chemistry are biocompatible: in vitro and in vivo assessment, J. Biochem. Mol. Toxicol. 33 (2019) e22291, https://doi.org/10.1002/jbt.22291.

[47] N.V. Skorodumova, S.I. Simak, B.I. Lundqvist, I.A. Abrikosov, B. Johansson, Quantum origin of the oxygen storage capability of ceria, Phys. Rev. Lett. 89 (16) (2002) 166601, https://doi.org/10.1103/PhysRevLett.89.166601.

[48] H. Jan, M.A. Khan, H. Usman, M. Shah, R. Ansir, S. Faisal, N. Ullah, L. Rahman, The *Aquilegia pubiflora* (Himalayan columbine) mediated synthesis of nanoceria for diverse biomedical applications, RSC Adv. 10 (33) (2020) 19219–19231, https://doi.org/10.1039/D0RA01971B.

[49] A. Butt, J.S. Ali, A. Sajjad, S. Naz, M. Zia, Biogenic synthesis of cerium oxide nanoparticles using petals of *Cassia glauca* and evaluation of antimicrobial, enzyme inhibition, antioxidant, and nanozyme activities, Biochem. System. Ecology 104 (2022) 104462, https://doi.org/10.1016/j.bse.2022.104462.

[50] M. Abdel-Nasser, G. Abdel-Maksoud, M.S. Abdel-Aziz, S.S. Darwish, A.A. Hamed, A.M. Youssef, Evaluation of the efficiency of nanoparticles for increasing α-amylase enzyme activity for removing starch stain from paper artifacts, J. Cultur. Herit. 53 (2022) 14–23, https://doi.org/10.1016/j.culher.2021.11.004.

[51] K. Saware, R.M. Aurade, P.D.K. Jayanthi, V. Abbaraju, Modulatory effect of citrate reduced gold and biosynthesized silver nanoparticles on α-amylase activity, J. Nanoparticles (2015) 829718, https://doi.org/10.1155/2015/829718.

[52] K.R. Sangeetha Gowda, B.B. Mathew, C.N. Sudhamani, H.S. Bhojya Naik, Mechanism of DNA binding and cleavage, Biomed. Biotech. 2 (1) (2014) 1–9.

[53] P. Maleki, F. Nemati, A. Gholoobi, A. Hashemzadeh, Z. Sabouri, M. Darroudi, Green facile synthesis of silver-doped cerium oxide nanoparticles and investigation of their cytotoxicity and antibacterial activity, Inorg. Chem. Commun. 131 (2021) 108762, https://doi.org/10.1016/j.inoche.2021.108762.

[54] N. Pandiyan, B. Murugesan, J. Sonamuthu, S. Samayanan, S. Mahalingam, [BMIM] PF6 ionic liquid mediated green synthesis of ceramic SrO/CeO_2 nanostructure using *Pedalium murex* leaf extract and their antioxidant and antibacterial activities, Ceramic Int 45 (9) (2019) 12138–12148, https://doi.org/10.1016/j.ceramint.2019.03.116.

[55] B. Zhu, X. Xia, N. Xia, S. Zhang, X. Guo, Modification of fatty acids in membranes of bacteria: ımplication for an adaptive mechanism to the toxicity of carbon nanotubes, Environ. Sci. Technol. 48 (7) (2014) 4086–4095, https://doi.org/10.1021/es404359v.

[56] L. Wang, C. Hu, L. Shao, The antimicrobial activity of nanoparticles: present situation and prospects for the future, Int. J. Nanomed. 12 (2017) 1227–1249.

[57] M. Zhuo, J. Ma, X. Quan, Cytotoxicity of functionalized CeO_2 nanoparticles towards Escherichia coli and adaptive response of membrane properties, Chemosphere 281 (2021) 130865, https://doi.org/10.1016/j.chemosphere.2021.130865.

[58] E. Maunders, M. Welch, Matrix exopolysaccharides; the sticky side of biofilm formation, FEMS (Fed, Eur. Microbiol. Soc.) Microbiol. Lett. 364 (13) (2017) 120, https://doi.org/10.1093/FEMSLE/FNX120.

[59] H.C. Flemming, J. Wingender, The biofilm matrix, Nat. Rev. Microbiol. 8 (2010) 623–633, https://doi.org/10.1038/nrmicro2415.

[60] M. Altaf, S. Manoharadas, M.T. Zeyad, Green synthesis of cerium oxide nanoparticles using *Acorus Calamus* extract and their antibiofilm activity against bacterial pathogens, Microsc. Res. Tech. 84 (2021) 1638–1648, https://doi.org/10.1002/jemt.23724.
[61] S.N. Naidi, F. Khan, A.L. Tan, M.H. Harunsani, Y.-M. Kim, M.M. Khan, Photoantioxidant and antibiofilm studies of green synthesized Sn-doped CeO_2 nanoparticles using aqueous leaf extracts of *Pometia pinnata*, New J. Chem. 45 (2021) 7816–7829, https://doi.org/10.1039/D1NJ00416F.
[62] A. Iqbal, T. Ahamad, F. Abul Qais, N. Ahmad, A. Shafi, A.S. Ahmed, S. Srivastava, Proficient visible-light-driven photocatalytic and anti-biofilm activity of biosynthesized CeO_2-graphene oxide nanocomposites, Mater. Chem. Phys. 298 (2023) 127397, https://doi.org/10.1016/j.matchemphys.2023.127397.